Published in final edited form as:
Neuroinformatics. 2013 January ; 11(1): 35–45. doi:10.1007/s12021-012-9163-0.

Automated Segmentation of Mouse Brain Images Using Multi-Atlas Multi-ROI Deformation and Label Fusion

Jingxin Nie and **Dinggang Shen**
Department of Radiology and BRIC, University of North Carolina at Chapel Hill, School of Medicine, MRI Building, CB #7513, 106 Mason Farm Road, Chapel Hill, NC 27599, USA

Jingxin Nie: niejingxin@gmail.com; Dinggang Shen: dinggang_shen@med.unc.edu

Abstract

We propose an automated multi-atlas and multi-ROI based segmentation method for both skull-stripping of mouse brain and the ROI-labeling of mouse brain structures from the three dimensional (3D) magnetic resonance images (MRI). Three main steps are involved in our method. First, a region of interest (ROI) guided warping algorithm is designed to register multi-atlas images to the subject space, by considering more on the matching of image contents around the ROI boundaries which are more important for ROI labeling. Then, a multi-atlas and multi-ROI based deformable segmentation method is adopted to refine the ROI labeling result by deforming each ROI surface via boundary recognizers (i.e., SVM classifiers) trained on local surface patches. Finally, a local-mutual-information (MI) based multi-label fusion technique is proposed for allowing the atlases with better local image similarity with the subject to have more contributions in label fusion. The experimental results show that our method works better than the conventional methods on both in vitro and in vivo mouse brain datasets.

Keywords

Mouse brain images; Segmentation; Multi-atlases; Multi-ROIs; Deformable segmentation; Label fusion

Introduction

Mouse models have been widely used for understanding human diseases, testing drugs, and evaluating therapies. Several researchers have adopted high-resolution 3D MRI to measure the morphometry of mouse brain models (McDaniel et al. 2001; Redwine et al. 2003; Spring et al. 2007; Nieman et al. 2007; Lau et al. 2008; Lerch et al. 2008; Zhang et al. 2010). Specifically, by morphological analyses of mouse brain MRI, the longitudinal development of brain atrophy in Huntington's disease mouse models (Lerch et al. 2008; Zhang et al. 2010) and Alzheimer's disease mouse models (Lau et al. 2008) can be quantified. Also, the volumetric changes of mouse brain can be tracked (McDaniel et al. 2001; Redwine et al. 2003).

Although the automated methods for human brain MRI segmentation have been studied for decades, the automated segmentation of mouse brain images has not received too much attention (Ali et al. 2005; Badea et al. 2007; Zhang et al. 2010). However, manual or semi-automatic labeling of mouse brain structures is both time-consuming and error prone,

Correspondence to: Dinggang Shen, dinggang_shen@med.unc.edu.

although this type of methods were well adopted in the previous morphometric studies of mouse brains (Badea et al. 2007; McDaniel et al. 2001; Redwine et al. 2003; Zhang et al. 2010). On the other hand, several automated segmentation methods for mouse brain images (Ali et al. 2005; Wu et al. 2006; Lau et al. 2008; Lerch et al. 2008; Sharief et al. 2008; Bae et al. 2009; Lee et al. 2009) have been proposed recently. In these methods, an atlas or a manually-labeled image is first nonlinearly registered onto the subject according to the matching of image intensities. Then, the subject image is segmented based on the warped label (or ROI) information. In these methods, typically the image registration is performed by considering all voxels in the whole images equally, and only one atlas (i.e., a labeled subject or the statistical classifiers built from multiple atlases) is typically used during registration. Recently, multi-atlas fusion methods have been studied extensively in the medical image analysis field, to avoid both bias and potential inaccurate registration from the single atlas (Sabuncu et al. 2010; Chakravarty et al. 2012). For effective mouse brain segmentation, multi-atlas fusion technique has also been investigated and better result was achieved compared to the single atlas based techniques (Chakravarty et al. 2012).

Meanwhile, deformable models are widely adopted for biomedical image segmentation (Chakraborty et al. 1996; Liu et al. 2008; McInerney and Terzopoulos 1996; Shen et al. 1999; Zhan and Shen 2006). In (Chakraborty et al. 1996; Liu et al. 2008), local intensity information and structured surface shape are combined to identify the object boundaries. In (Zhan and Shen 2006), a deformable segmentation method is proposed to segment 3D ultrasound prostate images using statistical classifiers to learn boundary information locally. However, deformable model usually requires a good initialization close to the expected boundary (Chakraborty et al. 1996; Liu et al. 2008; McInerney and Terzopoulos 1996; Zhan and Shen 2006), in order to achieve the robust segmentation results.

To solve these problems, we propose a deformable label fusion method that combines multi-atlas multi-ROIs information. Specifically, a ROI-guided warping algorithm is first proposed to register each atlas to the subject by considering more on the matching of image contents around the ROI boundaries, which are more important for ROI labeling. Then, a multi-atlas and multi-ROI based deformable segmentation method is adopted to refine the ROI labeling result by deforming ROI surface via the boundary recognizers (i.e., SVM classifiers) trained on local surface patches. In this step, the surface is reconstructed for each ROI in each atlas, and then is parcellated into small patches by local appearance similarity using normalized cut method (Shi and Malik 2000). After that, a SVM model is further trained on each patch to learn local ROI appearance information that contains the local image information from multiple atlases. Finally, the ROI surface is deformed in the subject space to locate the ROI boundaries guided by the respectively trained SVMs that can classify local regions as ROI or non-ROI labels. To obtain better segmentation results, multiple atlases are used to avoid the bias from the use of a single atlas, and also a local mutual information (MI) based multi-label fusion technique is developed for allowing the atlases with better local image similarity with the subject to have more contributions in label fusion. We have successfully applied this method to the structure-labeling of both in vitro and in vivo mouse brain images.

Method

Overview

An overview of our automated mouse brain segmentation pipeline is shown in Fig. 1. This automated atlas-based segmentation method can be applied to both skull-stripping of mouse brain and the ROI-labeling of mouse brain structures. Before using this pipeline for mouse brain skull-stripping and ROI-labeling, intensity inhomogeneity of each new subject image

is first corrected (Sled et al. 1998) and then the global intensity distribution is matched with those of atlas images.

For skull-stripping of a new subject image, each atlas image is first affine registered to the subject image. By defining the whole brain in each atlas as a big ROI, each atlas image can be warped to the subject using a ROI-guided registration approach as detailed below. Then, the surface is reconstructed for each ROI in each atlas, and further parcellated into a set of small patches according to local appearance similarity by using normalized cut method (Shi and Malik 2000). After that, a SVM model is trained on each patch to learn local ROI appearance information that contains the local image information from multiple atlases. Thus, the ROI surface can be deformed in the subject space to locate the ROI boundaries, guided by the respectively trained SVMs that can classify local regions as ROI or non-ROI labels. Finally, we can use our local-MI-based multi-label fusion technique to segment the subject image into brain and non-brain regions.

The same method described above can also be used for ROI labeling of brain structures as illustrated in Fig. 1b. By focusing on the ROI boundaries of each atlas, the ROI-guided registration method is performed to register each skull-stripped atlas image with the skull-stripped subject image by emphasizing the matching of ROI boundaries during the registration, which is the most important for ROI labeling. Then, after registration, a multi-atlas and multi-ROI based deformable segmentation method is adopted to refine the ROI labeling result by deforming each ROI surface via its respective boundary recognizers (i.e., SVM classifiers) trained on local surface patches. Finally, the local-MI-based multi-label fusion technique is applied to the multiple warped atlases for obtaining the final segmentation result.

ROI-guided Registration

For ROI-based segmentation methods, accurate registration between atlas and subject images is critical for achieving good segmentation results. Although accurate registration would be preferred for all image voxels, good registration of images around the ROI boundaries is more important and directly related to the segmentation results. Although it is good to have the images within the ROIs also being registered, their registration does not directly contribute to the segmentation results. In contrast, putting more effort on the registration of images within ROIs may affect the registration of images around ROI boundaries, thus eventually affecting the segmentation results. To this end, a ROI-guided warping algorithm is proposed in this paper for registering each atlas to the subject by considering more on the matching of images around the ROI boundaries, which are more important for ROI labeling.

Specifically, diffeomorphic Demons framework (Vercauteren et al. 2009), which has been proved to be an efficient registration method for mouse brain (Lee et al. 2009), is adopted in this paper. Given an atlas image I_A and a subject image I_S, their registration can be formulated as finding a deformation field f to minimize an energy function as defined below:

$$\min_f Diff(I_S(\boldsymbol{x}), I_A(f(\boldsymbol{x}))) + Reg(f(\boldsymbol{x})) \quad (1)$$

where $Diff(\cdot)$ measures the difference between two images and $Reg(\cdot)$ is the regularization term on the estimated deformation field $f(\boldsymbol{x})$. These two terms are defined in Demons as $Diff(I_S(\boldsymbol{x}), I_A(f(\boldsymbol{x}))) = \|\frac{1}{\sigma_i}(I_S(\boldsymbol{x}) - I_A(f(\boldsymbol{x})))\|^2$ and $Reg\, Reg(f(\boldsymbol{x})) = \|\frac{1}{\sigma_T}\nabla f(\boldsymbol{x})\|^2$, where σ_i accounts for the noise in the image intensities, and σ_T controls the amount of regularization on deformation field $f(\boldsymbol{x})$.

The solution to this energy minimization problem can be obtained by iteratively updating deformation field $f(x)$ (Vercauteren et al. 2009). For example, given a current deformation field $f(x)$, the corresponding compositive update u on each voxel x can be defined as below:

$$u(x)=-\kappa(f(x))\frac{I_S(x)-I_A(f(x))}{\left\|J(x)\right\|^2+\frac{\sigma_i^2}{\sigma_T^2}}J(x)^T \quad (2)$$

where $\kappa(f(x))$ is a weight function measuring the importance of the voxel x in the atlas image I_A during the registration. When $\kappa(f(x))=1$, u in Eq. (2) becomes a regular update vector in the Demons registration method (Vercauteren et al. 2009). $J(x)$ is the gradient of image I_S or $I_A(f)$, or even the average of both gradients at voxel x.

Assume that R_A is the corresponding ROI (or label) map of the atlas image I_A. Thus, we can define its weight function $\kappa(f(x))$ in the entire image space as:

$$\kappa(f(x))=\begin{cases}\kappa_1, & \left\|\nabla R_A(f(x))\right\|>0\\ \kappa_2, & \left\|\nabla R_A(f(x))\right\|=0\end{cases} \quad (3)$$

Where $\|\nabla R_A(f(x))\|$ is the magnitude of gradient of ROI map R_A at voxel $f(x)$; κ_1 and κ_2 are the two different weighting values used to control the amount of deformation in the boundary regions and other non-boundary regions, respectively. By setting $\kappa_1 \geq \kappa_2$, the ROI boundary regions will deform and arrive at their correspondences in the subject space faster than these non-boundary regions.

Multi-atlas and Multi-ROI Based Deformable Segmentation

Since non-linear registration in the previous step provides a good estimation of ROI labels especially for the ROIs with strong boundaries, deformable models can use these labels as good initializations to further refine the ROI labeling results. As for the ROIs with weak boundaries, their registration and labeling can be guided by the nearby ROIs with strong boundaries. Meanwhile, multiple atlases could provide complementary shape and appearance information for each ROI. Thus, a deformable model guided by information learned from multiple atlases using statistical method (Zhan and Shen 2006) can be defined for each ROI of each atlas, and could further improve the ROI labeling results.

Specifically, a triangulated surface $S_{i,j}$ is firstly reconstructed for each ROI (j) in each atlas (i) to model the shape of the respective ROI. Then, the appearance model is reconstructed for each surface $S_{i,j}$ using local intensity information collected from multi-atlas images in the corresponding positions. After warping all surfaces to the subject space using the deformation field estimated from the ROI-guided registration method as proposed in the previous section, each surface $S_{i,j}$ can be deformed to the respective location by fitting the appearance model to the subject image under constraint of surface smoothness. Finally, all the deformed ROI surfaces from the same atlas can be combined together as the final segmentation result. All results by different atlases will be further fused together as described below, to produce the final segmentation result for the subject.

Surface Model Reconstruction—For each ROI (j) in each atlas (i), a triangulated surface $S_{i,j}$ is reconstructed using Marching Cubes method (Lorensen and Cline 1987), and then it is parcellated into a set of small patches, along with the support vector machine (SVM) trained on each patch to obtain local appearance information in the image.

Surface Parcellation: In mouse brain image, most ROIs are connected to multiple other ROIs in the neighborhood. Thus, local image intensity information along each ROI boundary could be different, depending on which other ROIs it is connected with. In this way, each ROI surface $S_{i,j}$ should also be characterized locally. On the other hand, although we can define a SVM model for each vertex of ROI surface $S_{i,j}$, it is time-consuming to train a large number of SVMs (due to the large number of vertices in each surface $S_{i,j}$) and also it could be very sensitive to noise in the local region around each vertex. Thus, a compromising method is to partition each surface into a set of small patches, with each patch having the similar appearance on the respective vertices. In our implementation, the normalized cut method (Shi and Malik 2000) is adopted to partition a surface into several partitions of vertex set with high appearance similarity within same partition, while low appearance similarity between different partitions.

Specifically, the normalized cut method will firstly partition an undirected graph into two sub-graphs and then further partition each sub-graph iteratively into small patches. Given a weighted graph $G=(V, E)$, let V_1 and V_2 are the two complementary partitions of vertex set V, and the partition problem could be defined as minimizing the similarity between different partitions and maximizing the similarity within the same partition. Here, the similarity between two partitions $n_c(V_1, V_2)$ and the similarity within two partitions $n_a(V_1, V_2)$ can be defined as below, respectively:

$$n_c(V_1, V_2)=\frac{S(V_1, V_2)}{S(V_1, V)}+\frac{S(V_1, V_2)}{S(V_2, V)} \quad (4)$$

$$n_a(V_1, V_2)=\frac{S(V_1, V_1)}{S(V_1, V)}+\frac{S(V_2, V_2)}{S(V_2, V)} \quad (5)$$

The similarity between two partitions V_i and V_j, $S(V_i, V_j)$, is defined as:

$$S(V_i, V_j)=\sum_{v_k\in V_i, v_l\in V_j} s_{v_k, v_l} \quad (6)$$

where $s_{vk, vl}$ is the appearance similarity between vertices v_k and v_l. Since $n_c(V_1, V_2) = 2-n_a(V_1, V_2)$, the minimization of $n_c(V_1, V_2)$ is also equal to the maximization of $n_a(V_1, V_2)$. Since the problem is a NP-hard problem, the spectral method is adopted here to find a solution (Shi and Malik 2000).

In our implementation, the similarity between different vertices is defined as a combination of similarity of local normal direction and also the similarity of intensity information. Specifically, the local intensity feature vector of each vertex v_k at position $\mathbf{x}\ v_k$ is first defined as the intensity values sampled along the normal direction of this vertex:

$$Fea(\boldsymbol{x}_{v_k})=(I_A(\boldsymbol{x}_{v_k}-\lambda\boldsymbol{n}_{v_k}), \cdots, I_A(\boldsymbol{x}_{v_k}), \cdots, I_A(\boldsymbol{x}_{v_k}+\lambda\boldsymbol{n}_{v_k})) \quad (7)$$

where $\boldsymbol{n}_{v_k}$ is the normal direction of the vertex v_k, and $2\lambda+1$ is the length of feature vector. An example of this sampling along normal direction is shown in Fig. 2(a), e.g., sampling for a vertex (green) of ROI surface (white) along the normal direction (red line). Then, the similarity between the two neighboring vertices v_k and v_l could be defined as:

$$s_{v_k,v_l}=w_1\cdot\left(1-\frac{\left\|Fea(\boldsymbol{x}_{v_k})-Fea(\boldsymbol{x}_{v_l})_2\right\|}{(2\lambda+1)\cdot\max(\left\|Fea(\boldsymbol{x}_{v_k})\right\|_\infty, \left\|Fea(\boldsymbol{x}_{v_l})\right\|_\infty)}\right)+w_2\cdot(\boldsymbol{n}_{v_k}\cdot\boldsymbol{n}_{v_l})\left(1-\frac{\left\|\boldsymbol{x}_{v_k}-\boldsymbol{x}_{v_l}\right\|_2}{\max_{v_i,v_j\in V}\left\|\boldsymbol{x}_{v_i}-\boldsymbol{x}_{v_j}\right\|_2}\right) \quad (8)$$

where $\boldsymbol{n}_{v_k}$ and $\boldsymbol{n}_{v_l}$ are the normal directions of two vertices v_k and v_l, respectively. The two weighting parameters w_1 and w_2 control the contributions of the intensity and geometric similarities, respectively. If the vertices v_k and v_l are not directly connected, their similarity is set to 0.

We expect each patch to have similar surface area. In our implementation, the average surface area for each patch is around 3 mm^2. One example of surface partition result is shown in Fig. 2(b), where different colors represent different surface patches.

Support Vector Machine Trained on Each Surface Patch: The ROI image appearance (Zhan and Shen 2003; Shi et al. 2008; Wang et al. 2001) could be characterized by comparing the local image features between ROI and non-ROI regions, as shown in Fig. 3, where the ROI region is marked by "+" and non-ROI region is marked by "−". SVM can estimate a decision plane to separate positive samples from negative samples based on the statistical learning theory. Compared to other classification methods, SVM can obtain the maximum generalization ability (Burges 1998) by maximizing the margin distance, instead of classification errors between classes. Thus, in our method, SVM model is trained to separate local ROI and non-ROI voxels for each surface patch $P_{i,j,k}$.

As shown in Fig. 3, each patch $P_{i,j,k}$ in the atlas i is first deformed to the other atlas images using the deformation field generated by registration of other atlases' label images to the selected atlas' label image. Then image features are extracted for each vertex in the surface patch (and also its neighboring voxels) from all atlas images, which include the image intensity information along normal direction as described in Eq. (7) and also the local intensity gradient vector. An example is shown in Fig. 3, where the local image features and the corresponding labels for the vertices in the light-blue surface patch are extracted from all atlas images and used as the sample dataset to train the SVM model.

For the simplicity, the linear SVM model is adopted in our method, instead of non-linear SVM model. 90% of data is randomly selected from the sample dataset to train the SVM model, and the rest dataset is used as the testing samples to measure the classification accuracy of each SVM model as shown in Fig. 3. Since the features extracted from image might be not good enough to separate ROI and non-ROI regions, such as ROI and non-ROI regions with similar image intensity, the SVM model might not be able to distinguish between them, such as the blue surface patch shown in Fig. 3, which has similar image intensity inside and outside the patch boundaries. To reduce the possibility of misguidance by the low-accuracy classifiers, only the SVM models with the accuracy higher than 75% are used in the later stage to refine the labeling boundaries.

SVM-guided Surface Deformation—After construction of SVM model on each surface patch, the whole surface can be deformed in the subject space to locate the respective ROI boundaries, guided by the trained SVM that can classify the local regions as ROI and non-ROI labels, respectively.

The deformable model introduced in (Kass et al. 1988; McInerney and Terzopoulos 1996; Shen and Ip 1997) is adopted in this paper. It deforms a parameterized surface in the spatial domain by following the internal $\boldsymbol{F}_{int}$ and external $\boldsymbol{F}_{ext}$ forces as described:

$$\frac{dv}{dt} = \boldsymbol{F}_{int} + \boldsymbol{F}_{ext} \quad (9)$$

where the surface vertex v is treated as a function of time t. Usually the internal force is used to smooth the deformed surface and/or restore it to the original configuration; thus, in our

implementation, the internal force is simply defined to smooth the locations of vertices around each vertex in the surface patch. Specifically, the internal force deforms the vertex to the center of its neighboring vertices.

The external force is used to deform the surface to the expected ROI boundary. Since the SVM model in our method can classify the local region and identify the rough boundary locally, the external force can be calculated by the local SVM classification results. Specifically, for each vertex v in the surface patch, the local classification results in its spherical neighborhood can be obtained by applying SVM model on the respective feature vectors, and the external force can thus be defined as:

$$\boldsymbol{F}_{ext}(v)=\frac{\sum_{\forall \boldsymbol{x}_i \in \boldsymbol{N}(v)} L(v, \boldsymbol{x}_i)}{\sum_{\forall \boldsymbol{x}_i \in \boldsymbol{N}(v)} 1} \cdot \boldsymbol{n}_v \quad (10)$$

where $L(v,x_i)$ is the classification result of voxel x_i in the spherical neighborhood $N(v)$ of the surface vertex v, and $\boldsymbol{n}_v$ is the normal direction of vertex v. When $L(v, x_i) =1$, it indicates that the voxel x_i could be in the ROI region, and $L(v, i)=-1$ indicates that the voxel x_i could be in the non-ROI region. Thus, if vertex v is inside the ROI region, more voxels are classified as ROI region, and the direction of $\boldsymbol{F}_{ext}$ will be the same as the normal direction of the surface patch as shown in Fig. 4.

After deforming each vertex to its final position as described in the Section “SVM-guided Surface Deformation”, ROIs from the same atlas could be combined as a whole segmentation result. However, since each ROI is deformed independently, there might exist certain overlap or gap between the two deformed ROIs with surface-based deformation. To deal with this issue, the ROI labels at the overlapping or gap regions are estimated by the minimal distance criterion. As shown in Fig. 5, the red voxel in the overlapping region can be labeled as ROI 2, since its distance (d_2) to ROI 2 is smaller than its distance (d_1) to ROI 1.

MI-based Multi-atlas Label Fusion

Further fusion of multiple deformed atlases could reduce the bias of segmentation caused by the single atlas-based segmentation (Sabuncu et al. 2010), and might also overcome the possible failure during the single atlas-based segmentation.

Given a subject image I_S, all N atlas images $\{I_i(\boldsymbol{x}), i=1, 2, \ldots, N\}$ can be warped to the subject space $\{I_i(f_i(\boldsymbol{x})), i=1, 2, \ldots, N\}$, respectively. The warped ROI labels of these atlases can be obtained as $\{ R_i^{'}, i - 1, 2 \ldots, \boldsymbol{N}\}$ by using the methods described in the previous sections. Now, the problem becomes how to fuse the multi-labels from multiple atlases to achieve a good segmentation $\hat{R}_S$ for the subject I_S.

It is expected that the atlases with better local alignment with the subject should have more contributions for the label fusion of each voxel x in the subject. The local alignment degree between the atlas image I_i and the subject I_S at voxel x can be defined by their mutual information (MI) as:

$$m_i(\boldsymbol{x})=MI(I_i^{Nbr}(\boldsymbol{f}_i(\boldsymbol{x})), I_S^{Nbr}(\boldsymbol{x})) \quad (11)$$

where $I_s^{\boldsymbol{Nbr}}(x)$ is the neighborhood of voxel $\boldsymbol{x}$ in the subject image I_S, and $MI(\cdot, \cdot)$ is the MI between the two image regions.

Thus, the local-MI-based segmentation for each voxel $\boldsymbol{x}$ in the subject can be described to find a label $\hat{R}_S(\boldsymbol{x})$ which maximizes the similarity between the label $\hat{R}_S(\boldsymbol{x})$ and the labels $R_I'(\boldsymbol{x})$ from all atlases:

$$\widehat{R}_S(\boldsymbol{x}) = \arg\max_{R(\boldsymbol{x})} \sum_{i=1}^{N} m_i(\boldsymbol{x})\delta(R(\boldsymbol{x}) - R_i'(\boldsymbol{x})) \quad (12)$$

where $\delta(\cdot)$ is the Dirac delta function, and m_i denotes the weight for atlas i. When m_i is set as constant for all atlases, the segmentation will be the simple majority voting.

Image Datasets and Atlases

The Brookhaven's C57BL/6J mouse database (Ma et al. 2005), which includes both in vitro and in vivo atlases, is adopted in our experiments. For in vitro data, T2-weighted MRIs were acquired from 10 C57BL/6J mouse with size of 256×256×512 voxels and isotropic 0.047 mm spacing. For in vivo data, T2-weighted MRI images were acquired from 12 C57BL/6J mouse with size of 192×96×256 voxels and isotropic 0.10 mm spacing.

To create individual atlases, one of the images was firstly manually segmented into 20 ROIs. Then, this image was registered to other images for guiding the respective segmentations. Finally, all these segmentation results were manually refined to build the final atlases.

Results

In the experiments, we use the leave-one-out cross-validation to evaluate the performance of skull-stripping and ROI labeling. Also, parameters are set as κ_1=1.5, κ_2=0.5, λ=10, w_1=0.5, w_2=0.5, σ_i=1, σ_T=1 and α=0.5 in all experiments that are reported below. The experiments were performed in a PC with Intel core i5 2.67 GHz CPU. The average labeling time with 9 atlases is about 30 min for in-vivo image, and 2 h for in-vitro image.

Skull Stripping

We used Dice ratio to measure the overlay of our skull-stripping result and manual skull-stripping result on all in vivo images. As reported in Table 1, compared with the original Demons registration method, our ROI-guided registration method improves the average Dice ratio from 0.909 to 0.928 when using single-atlas-based segmentation. After using SVM-based deformable segmentation, the average Dice ratio increases from 0.928 to 0.975. Finally, after fusing all segmentation results by the local-MI-based multi-label fusion technique, the average Dice ratio increases from 0.975 to 0.980, which could be considered as a good result even compared to the skull-stripping result of human brain images (Lee et al. 2003; Park and Lee 2009; Smith 2002).

ROI Labeling

An example of ROI labeling result is shown in Fig. 6. After ROI-guided image registration, ROI labels are roughly matched with the ground-truth labels, but the boundary of one small ROI is not well matched, as indicated by the red arrow in Fig. 6. After using multi-atlas and multi-ROI based deformable segmentation, the labeling result is refined especially on the white ROI indicated by the red arrow in Fig. 6. By fusing label information from multiple atlases, the labeling result is further improved as shown in Fig. 6.

To quantitatively measure the accuracy of labeling, the Dice ratio is first used to compare our ROI-labeling results with manual ROI-labeling results on all in vitro and in vivo mouse images. The average Dice ratios of 20 ROIs for in vitro and in vivo mouse images are shown in Tables 2 and 3, respectively.

For in vitro dataset, our ROI-labeling method produces quite good results, with average Dice ratio of 0.904. The significant improvement by our multi-label fusion technique appears in the small ROIs such as anterior commissure (about 1.1 mm^3) which increases from 0.572 to 0.709, and ventricles (about 1.6 mm^3) which increase from 0.682 to 0.795, as shown in Table 2. But when Dice ratio arrives at a relatively high value (such as for neocortex and cerebellum), the improvement is limited.

For in vivo dataset, the ROI-labeling results are similar to those for in vitro dataset, but with an overall lower Dice ratio (0.859 compared to 0.904) due to the lower image quality. The Dice ratios for the small ROIs are improved by both ROI-guided registration method and multi-label fusion technique. For example, the Dice ratio of anterior commissure is improved from 0.413 to 0.443 by the ROI-guided registration method and further to 0.494 by using the SVM-based deformable segmentation, and finally reaches 0.609 by the multi-label fusion method.

To further quantitatively measure the accuracy of labeling, we also used the average surface distance to compare our ROI-labeling results with manual ROI-labeling results on all in vitro and in vivo mouse images. The average distance of 20 ROIs for in vitro and in vivo mouse images are shown in Tables 4 and 5, respectively.

For in vitro dataset, our ROI-labeling method produces quite good results, with average distance of 0.019 mm. The significant improvement by our multi-label fusion technique appears in the small ROIs such as anterior commissure (about 1.1 mm^3) which decrease surface error from 0.086 to 0.041 mm, and ventricles (about 1.6 mm^3) which decrease surface distance from 0.048 to 0.021 mm, as shown in Table 4.

For in vivo dataset, the ROI-labeling results are similar to those for in vitro dataset, but with an overall higher average surface distance (0.028 mm compared to 0.019 mm) due to the lower image quality and resolution. The average surface distance for the small ROIs are improved by both the ROI-guided registration method and the multi-label fusion technique. For example, the average surface distance for the ventricle is improved from 0.103 mm to 0.098 mm by the ROI-guided registration method, further to 0.088 mm by using the SVM-based deformable segmentation, and finally reaches 0.044 mm by the multi-label fusion method.

Conclusion

An automated multi-atlas multi-ROI based segmentation method has been proposed in this paper for both skull-stripping of mouse brain and the ROI-labeling of mouse brain structures. The method has been applied to both in vitro and in vivo datasets and shows good performance. We will make a dedicated software package for this developed method, and will further make it freely available to the researchers and users through our website (http://bric.unc.edu/ideagroup/) as we have done for our other developed methods.

Information Sharing Statement

We will make a dedicated software package for this developed method freely available to the researchers and users through our website (http://bric.unc.edu/ideagroup/).

Acknowledgments

This work was supported in part by NIH grants EB006733, EB008374, EB009634, AG041721, and CA140413, by National Science Foundation of China under grant No. 61075010, and also by The National Basic Research Program of China (973 Program) grant No. 2010CB732505.

References

Ali AA, Dale AM, Badea A, Johnson GA. Automated segmentation of neuroanatomical structures in multispectral MR microscopy of the mouse brain. NeuroImage. 2005; 27:425–435. [PubMed: 15908233]

Badea A, Nicholls PJ, Johnson GA, Wetsel WC. Neuroanatomical phenotypes in the reeler mouse. NeuroImage. 2007; 34:1363–1374. [PubMed: 17185001]

Bae MH, Pan R, Wu T, Badea A. Automated segmentation of mouse brain images using extended MRF. NeuroImage. 2009; 46:717–725. [PubMed: 19236923]

Burges CJC. A tutorial on support vector machines for pattern recognition. Data Mining and Knowledge Discovery. 1998; 2:121–167.

Chakraborty A, Staib LH, Duncan JS. Deformable boundary finding in medical images by integrating gradient and region information. IEEE Transactions on Medical Imaging. 1996; 15:859–870. [PubMed: 18215965]

Chakravarty MM, Steadman P, van Eede MC, Calcott RD, Gu V, Shaw P, Raznahan A, Collins DL, Lerch JP. Performing label-fusion-based segmentation using multiple automatically generated templates. Human Brain Mapping. 201210.1002/hbm.22092

Kass M, Witkin A, Terzopoulos D. Snakes: active contour models. International Journal of Computer Vision. 1988; 1:321–331.

Lau JC, Lerch JP, Sled JG, Henkelman RM, Evans AC, Bedell BJ. Longitudinal neuroanatomical changes determined by deformation-based morphometry in a mouse model of Alzheimer's disease. NeuroImage. 2008; 42(1):19–27. [PubMed: 18547819]

Lee J, Jomier J, Aylward S, Tyszka M, Moy S, Lauder J, Styner M. Evaluation of atlas based mouse brain segmentation. Proceedings of SPIE. 2009; 7259:725943–725949. [PubMed: 20640188]

Lee JM, Yoon U, Nam SH, Kim JH, Kim IY, Kim SI. Evaluation of automated and semi-automated skull-stripping algorithms using similarity index and segmentation error. Computers in Biology and Medicine. 2003; 33:495–507. [PubMed: 12878233]

Lerch JP, Carroll JB, Spring S, Bertram LN, Schwab C, Hayden MR, Henkelman RM. Automated deformation analysis in the YAC128 Huntington disease mouse model. NeuroImage. 2008; 39(1): 32–39. [PubMed: 17942324]

Liu T, Nie J, Tarokh A, Guo L, Wong ST. Reconstruction of central cortical surface from brain MRI images: method and application. NeuroImage. 2008; 40:991–1002. [PubMed: 18289879]

Lorensen WE, Cline HE. Marching cubes: A high resolution 3D surface reconstruction algorithm. Computer Graphics. 1987; 21

Ma Y, Hof PR, Grant SC, Blackband SJ, Bennett R, Slatest L, McGuigan MD, Benveniste H. A three-dimensional digital atlas database of the adult C57BL/6J mouse brain by magnetic resonance microscopy. Neuroscience. 2005; 135:1203–1215. [PubMed: 16165303]

McDaniel B, Sheng H, Warner DS, Hedlund LW, Benveniste H. Tracking brain volume changes in C57BL/6J and ApoE-deficient mice in a model of neurodegeneration: a 5-week longitudinal micro-MRI study. NeuroImage. 2001; 14:1244–1255. [PubMed: 11707081]

McInerney T, Terzopoulos D. Deformable models in medical image analysis: a survey. Medical Image Analysis. 1996; 1:91–108. [PubMed: 9873923]

Nieman BJ, Lerch JP, Bock NA, Chen XJ, Sled JG, Henkelman RM. Mouse behavioral mutants have neuroimaging abnormalities. Human Brain Mapping. 2007; 28(6):567–575. [PubMed: 17437292]

Park JG, Lee C. Skull stripping based on region growing for magnetic resonance brain images. NeuroImage. 2009; 47:1394–1407. [PubMed: 19389477]

Redwine JM, Kosofsky B, Jacobs RE, Games D, Reilly JF, Morrison JH, Young WG, Bloom FE. Dentate gyrus volume is reduced before onset of plaque formation in PDAPP mice: a magnetic resonance microscopy and stereologic analysis. Proceedings of the National Academy of Sciences United States of America. 2003; 100:1381–1386.

Sabuncu MR, Yeo BT, Van Leemput K, Fischl B, Golland P. A generative model for image segmentation based on label fusion. IEEE Transactions on Medical Imaging. 2010; 29:1714–1729. [PubMed: 20562040]

Sharief AA, Badea A, Dale AM, Johnson GA. Automated segmentation of the actively stained mouse brain using multi-spectral MR microscopy. NeuroImage. 2008; 39:136–145. [PubMed: 17933556]

Shen D, Ip HHS. A Hopfield neural network for adaptive image segmentation: An active surface paradigm. Pattern Recognition Letters. 1997; 18(1):37–48.

Shen D, Wong W, Ip HHS. Affine-invariant image retrieval by correspondence matching of shapes. Image and Vision Computing. 1999; 17(7):489–499.

Shi JB, Malik J. Normalized cuts and image segmentation. IEEE Transactions on Pattern Analysis and Machine Intelligence. 2000; 22:888–905.

Shi Y, Qi F, Xue Z, Chen L, Ito K, Matsuo H, Shen D. Segmenting lung fields in serial chest radiographs using both population-based and patient-specific shape statistics. IEEE Transactions on Medical Imaging. 2008; 27(4):481–494. [PubMed: 18390345]

Sled JG, Zijdenbos AP, Evans AC. A nonparametric method for automatic correction of intensity nonuniformity in MRI data. IEEE Transactions on Medical Imaging on. 1998; 17:87–97.

Smith SM. Fast robust automated brain extraction. Human Brain Mapping. 2002; 17:143–155. [PubMed: 12391568]

Spring S, Lerch JP, Henkelman RM. Sexual dimorphism revealed in the structure of the mouse brain using three-dimensional magnetic resonance imaging. NeuroImage. 2007; 35(4):1424–1433. [PubMed: 17408971]

Vercauteren T, Pennec X, Perchant A, Ayache N. Diffeomorphic demons: efficient non-parametric image registration. NeuroImage. 2009; 45:S61–S72. [PubMed: 19041946]

Wang Y, Teoh EK, Shen D. Structure-adaptive B-snake for segmenting complex objects. International Conference on Image Processing 2001. 2001; 2:769–772.

Wu G, Qi F, Shen D. Learning-based deformable registration of MR brain images. IEEE Transactions on Medical Imaging. 2006; 25(9):1145–1157. [PubMed: 16967800]

Zhan Y, Shen D. Automated segmentation of 3D US prostate images using statistical texture-based matching method. Medical Image Computing and Computer-Assisted Intervention-MICCAI. 2003; 2003:688–696.

Zhan Y, Shen D. Deformable segmentation of 3-D ultrasound prostate images using statistical texture matching method. IEEE Transactions on Medical Imaging. 2006; 25:256–272. [PubMed: 16524083]

Zhang J, Peng Q, Li Q, Jahanshad N, Hou Z, Jiang M, Masuda N, Langbehn DR, Miller MI, Mori S, Ross CA, Duan W. Longitudinal characterization of brain atrophy of a Huntington's disease mouse model by automated morphological analyses of magnetic resonance images. NeuroImage. 2010; 49:2340–2351. [PubMed: 19850133]

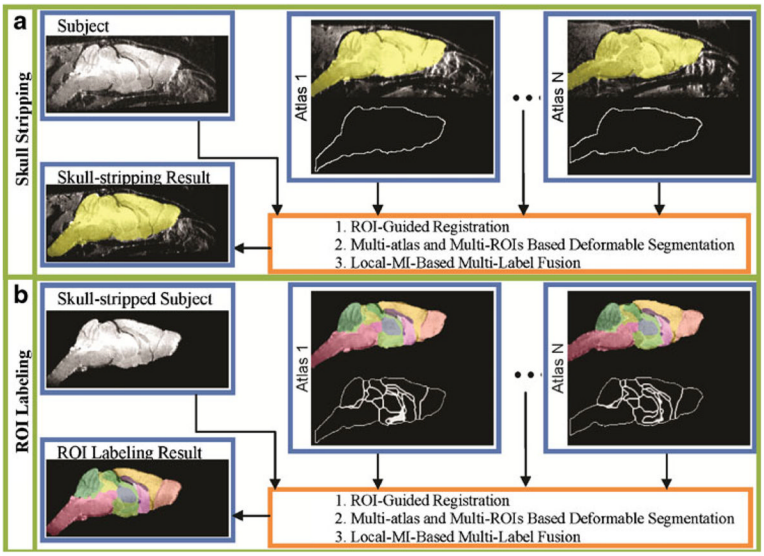

Fig. 1.
Mouse brain segmentation pipeline. **a** Skull stripping, and **b** ROI labeling

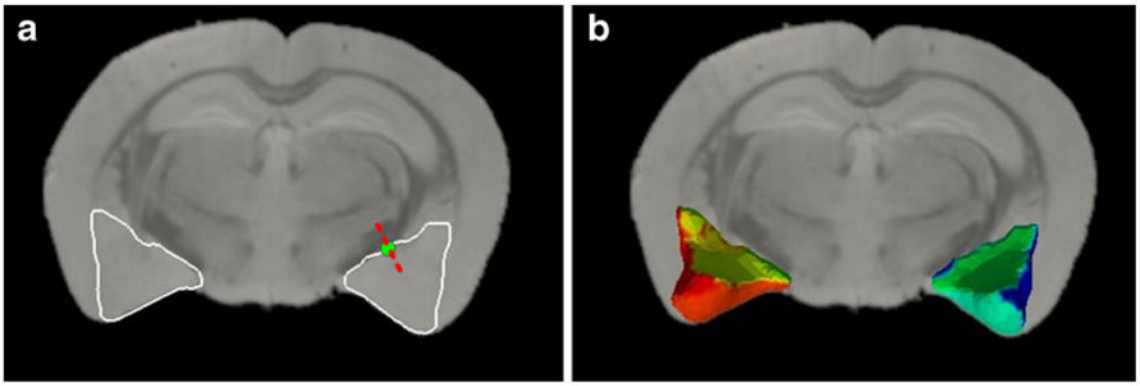

Fig. 2.
Example of surface parcellation. **a** A sample ROI surface with illustration on how to sample the intensity feature vector for each surface vertex. **b** The parcellation result for two ROI surfaces, where each color represents one surface patch

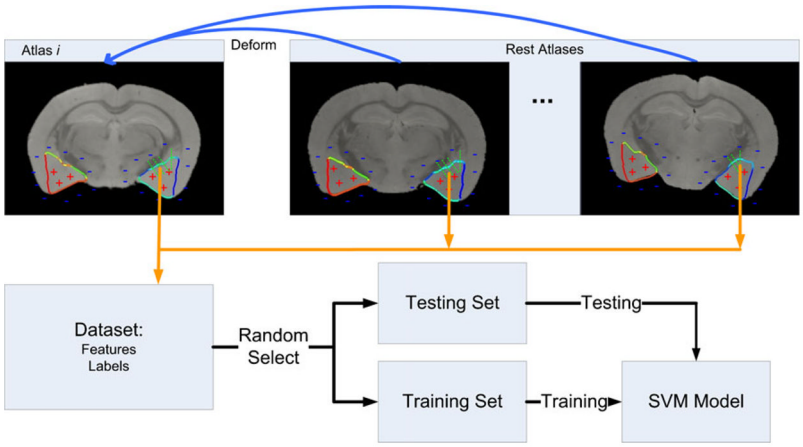

Fig. 3.

Flowchart of constructing support vector machine for each surface patch (i.e., *light-blue*). Each patch is first registered with the rest atlas images. Then the image features are extracted for each vertex in the surface patch from all atlas images. The sample dataset can thus be constructed. By dividing the sample dataset into the training and testing sets, we can train the SVM model and further test its performance

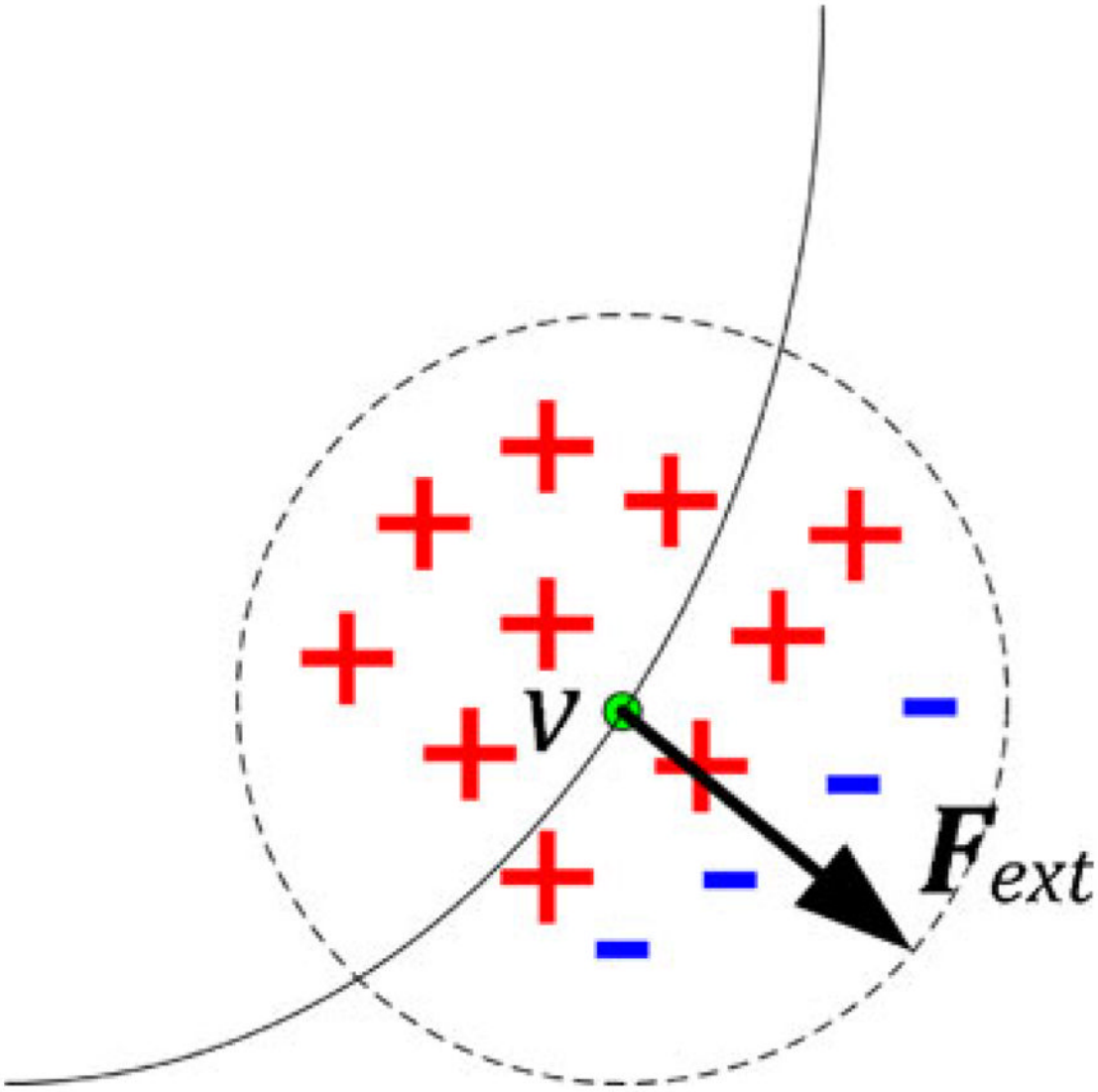

Fig. 4.
External force on vertex *v*, guided by the local classification results

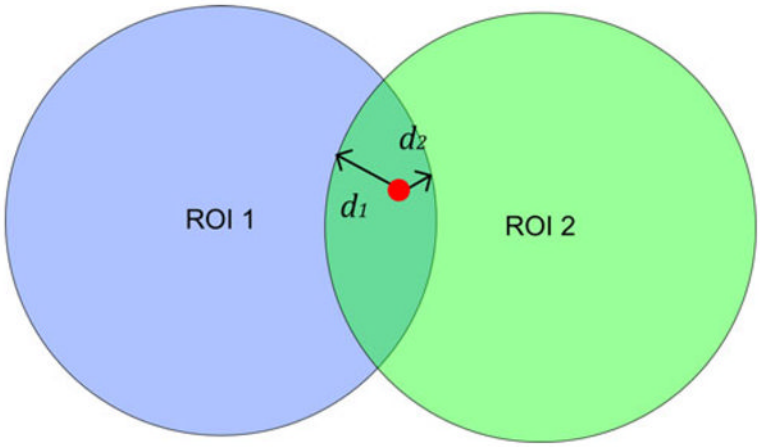

Fig. 5.
Illustration of re-labeling voxels in the overlapping region of ROIs

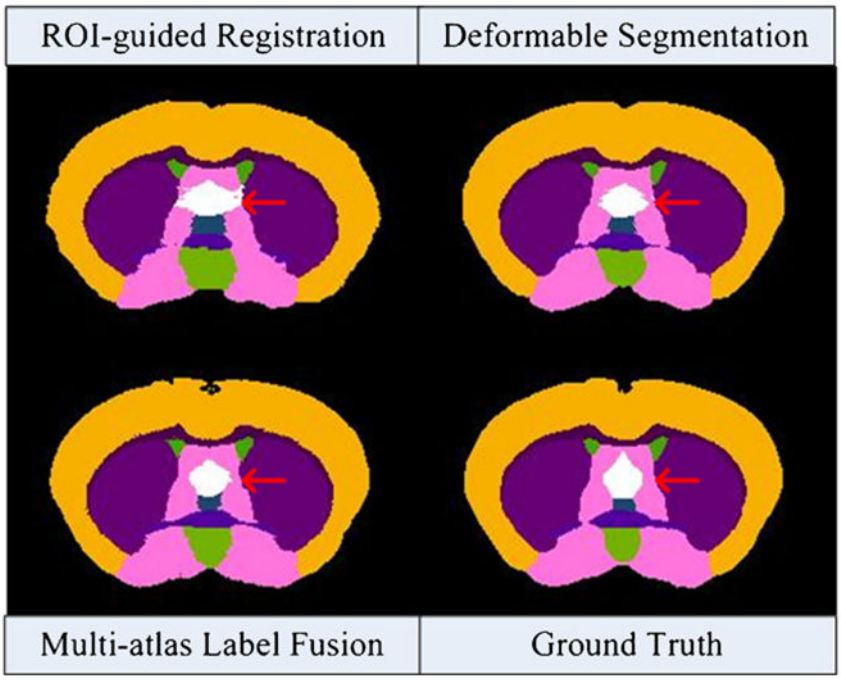

Fig. 6.
Illustration of mouse brain labeling results, compared to the ground truth

Table 1

Average Dice ratio (with standard deviation (STD)) for the skull-stripping results

Dice ratio (STD)	Diffeomorphic demons registration	ROI-guided registration	Deformable segmentation	Multi-atlas label fusion
Skull-stripping	0.909 (0.02)	0.928 (0.02) 0.975 (0.01)		0.980 (0.01)

Table 2

Average Dice ratio (with standard deviation (STD)) for the ROI-labeling results on in vitro dataset

Dice ratio (STD)	Diffeomorphic Demons registration	ROI-guided registration	Deformable segmentation	Multi-atlas label fusion
Hippocampus	0.927 (0.03)	0.922 (0.03)	0.936 (0.02)	0.943 (0.01)
External capsule	0.724 (0.05)	0.770 (0.05)	0.811 (0.05)	0.823 (0.05)
Caudate putamen	0.923 (0.01)	0.925 (0.01)	0.940 (0.01)	0.947 (0.01)
Anterior commisure	*0.572 (0.06)*	*0.561 (0.07)*	*0.651(0.05)*	*0.709 (0.05)*
Globus pallidus	0.845 (0.04)	0.852 (0.03)	0.878 (0.02)	0.901 (0.02)
Internal capsule	0.802 (0.05)	0.767 (0.05)	0.793 (0.04)	0.827 (0.03)
Thalamus	0.940 (0.02)	0.950 (0.01)	0.959 (0.01)	0.962 (0.01)
Cerebellum	0.930 (0.02)	0.928 (0.02)	0.941 (0.01)	0.966 (0.01)
Superior colliculi	0.906 (0.03)	0.915 (0.03)	0.932 (0.02)	0.936 (0.02)
Ventricles	*0.682 (0.08)*	*0.709 (0.07)*	*0.765(0.04)*	*0.795(0.04)*
Hypothalamus	0.903 (0.01)	0.931 (0.01)	0.954 (0.01)	0.943 (0.01)
Inferior colliculi	0.871 (0.08)	0.871 (0.08)	0.902 (0.03)	0.913 (0.02)
Central gray	0.883 (0.08)	0.896 (0.08)	0.914 (0.02)	0.918 (0.02)
Neocortex	0.933 (0.01)	0.940 (0.01)	0.951 (0.01)	0.965 (0.01)
Amygdala	0.884 (0.02)	0.889 (0.02)	0.926 (0.01)	0.931 (0.01)
Olfactory bulb	0.916 (0.02)	0.903 (0.02)	0.915 (0.02)	0.957 (0.01)
Brain stem	0.903 (0.02)	0.905 (0.02)	0.911 (0.02)	0.934 (0.01)
Rest of midbrain	0.873 (0.05)	0.897 (0.05)	0.927 (0.02)	0.933 (0.02)
Basal forebrain and septum	0.888 (0.03)	0.885 (0.03)	0.918 (0.02)	0.917 (0.02)
Fimbria	0.780 (0.05)	0.788 (0.05)	0.820 (0.03)	0.860 (0.03)
Overall average	0.854 (0.04)	0.860 (0.04)	0.887 (0.02)	0.904 (0.02)

Table 3

Average Dice ratio (with standard deviation (STD)) for the ROI-labeling results on in vivo dataset

Dice ratio (STD)	Diffeomorphic demons registration	ROI-guided registration	Deformable segmentation	Multi-atlas label fusion
Hippocampus	0.858 (0.03)	0.862 (0.03)	0.883 (0.02)	0.912 (0.02)
External capsule	0.628 (0.10)	0.636 (0.10)	0.645 (0.09)	0.717 (0.10)
Caudate putamen	0.871 (0.02)	0.871 (0.02)	0.900 (0.01)	0.920 (0.02)
Anterior commisure	*0.413 (0.06)*	*0.443(0.06)*	*0.494 (0.06)*	*0.609 (0.06)*
Globus pallidus	0.670 (0.04)	0.670 (0.04)	0.745 (0.02)	0.802 (0.02)
Internal capsule	0.579 (0.06)	0.582 (0.06)	0.630 (0.03)	0.715 (0.04)
Thalamus	0.889 (0.03)	0.892 (0.03)	0.910 (0.02)	0.929 (0.02)
Cerebellum	0.957 (0.01)	0.957 (0.01)	0.920 (0.01)	0.968 (0.01)
Superior colliculi	0.821 (0.06)	0.822 (0.06)	0.848 (0.04)	0.885 (0.05)
Ventricles	*0.631 (0.05)*	*0.644(0.06)*	*0.666 (0.05)*	*0.753(0.04)*
Hypothalamus	0.892 (0.03)	0.894 (0.03)	0.872 (0.03)	0.933 (0.02)
Inferior colliculi	0.809 (0.06)	0.808 (0.06)	0.838 (0.04)	0.885 (0.03)
Central gray	0.746 (0.08)	0.748 (0.08)	0.758 (0.09)	0.811(0.11)
Neocortex	0.945 (0.01)	0.945 (0.01)	0.903 (0.01)	0.965 (0.01)
Amygdala	0.860 (0.03)	0.861 (0.03)	0.832 (0.01)	0.911(0.01)
Olfactory bulb	0.965 (0.02)	0.964 (0.02)	0.897 (0.02)	0.980 (0.01)
Brain Stem	0.965 (0.02)	0.965 (0.02)	0.853 (0.02)	0.967 (0.02)
Rest of midbrain	0.785 (0.10)	0.789 (0.10)	0.817 (0.06)	0.863 (0.08)
Basal forebrain and septum	0.884 (0.02)	0.887 (0.02)	0.890 (0.01)	0.935 (0.01)
Fimbria	0.600 (0.11)	0.617 (0.11)	0.643 (0.04)	0.725 (0.04)
Overall average	0.788 (0.05)	0.793 (0.05)	0.797 (0.04)	0.859 (0.04)

Table 4

Average surface distance (mm), with standard deviation (STD) for the ROI-labeling results on in vitro dataset

Average distance (STD)	Diffeomorphic demons registration	ROI-guided registration	Deformable segmentation	Multi-atlas label fusion
Hippocampus	0.019 (0.004)	0.019 (0.004)	0.017 (0.003)	0.015 (0.003)
External capsule	0.025 (0.005)	0.024 (0.005)	0.017 (0.003)	0.015 (0.003)
Caudate putamen	0.020 (0.003)	0.019 (0.003)	0.015 (0.003)	0.013 (0.003)
Anterior commisure	0.086 (0.020)	0.078 (0.019)	0.060 (0.016)	0.041 (0.010)
Globus pallidus	0.023 (0.004)	0.024 (0.004)	0.018 (0.003)	0.014 (0.003)
Internal capsule	0.022 (0.004)	0.023 (0.004)	0.024 (0.004)	0.019 (0.003)
Thalamus	0.021 (0.004)	0.021 (0.004)	0.015 (0.003)	0.014 (0.003)
Cerebellum	0.038 (0.004)	0.037 (0.004)	0.031 (0.004)	0.015 (0.003)
Superior colliculi	0.023 (0.004)	0.023 (0.004)	0.018 (0.003)	0.017 (0.003)
Ventricles	0.048 (0.012)	0.047 (0.012)	0.037 (0.007)	0.021 (0.005)
Hypothalamus	0.026 (0.005)	0.025 (0.005)	0.013 (0.003)	0.016 (0.004)
Inferior colliculi	0.025 (0.004)	0.025 (0.004)	0.020 (0.003)	0.017 (0.003)
Central gray	0.026 (0.005)	0.025 (0.004)	0.019 (0.003)	0.018 (0.003)
Neocortex	0.021 (0.003)	0.021 (0.003)	0.016 (0.003)	0.010 (0.002)
Amygdala	0.026 (0.004)	0.026 (0.004)	0.017 (0.003)	0.015 (0.003)
Olfactory bulb	0.036 (0.005)	0.034 (0.005)	0.038 (0.006)	0.017 (0.003)
Brain stem	0.094 (0.020)	0.087 (0.018)	0.095 (0.020)	0.052 (0.013)
Rest of midbrain	0.029 (0.008)	0.028 (0.008)	0.017 (0.003)	0.015 (0.003)
Basal forebrain and septum	0.024 (0.004)	0.023 (0.004)	0.018 (0.004)	0.017 (0.003)
Fimbria	0.024 (0.004)	0.025 (0.004)	0.021 (0.004)	0.015 (0.003)
Overall average	0.033 (0.007)	0.032 (0.006)	0.026 (0.005)	0.019 (0.004)

Table 5

Average surface distance (mm), with standard deviation (STD) for the ROI-labeling results on in vivo dataset

Average distance (STD)	Diffeomorphic demons registration	ROI-guided registration	Deformable segmentation	Multi-atlas label fusion
Hippocampus	0.039 (0.008)	0.039 (0.008)	0.032 (0.007)	0.023 (0.006)
External capsule	0.046 (0.012)	0.047 (0.012)	0.048 (0.013)	0.036 (0.010)
Caudate putamen	0.030 (0.005)	0.031 (0.005)	0.027 (0.005)	0.021 (0.004)
Anterior commisure	0.082 (0.019)	0.080 (0.019)	0.085 (0.020)	0.068 (0.017)
Globus pallidus	0.054 (0.006)	0.057 (0.007)	0.047 (0.006)	0.033 (0.004)
Internal capsule	0.065 (0.008)	0.066 (0.008)	0.060 (0.008)	0.040 (0.005)
Thalamus	0.035 (0.006)	0.036 (0.006)	0.033 (0.004)	0.025 (0.004)
Cerebellum	0.039 (0.004)	0.031 (0.003)	0.034 (0.004)	0.013 (0.002)
Superior colliculi	0.050 (0.009)	0.050 (0.009)	0.042 (0.007)	0.031 (0.006)
Ventricles	0.103 (0.018)	0.098 (0.017)	0.088 (0.015)	0.044 (0.011)
Hypothalamus	0.033 (0.006)	0.030 (0.006)	0.032 (0.006)	0.016 (0.003)
Inferior colliculi	0.049 (0.008)	0.047 (0.008)	0.035 (0.005)	0.024 (0.004)
Central gray	0.057 (0.017)	0.058 (0.017)	0.055 (0.017)	0.039 (0.012)
Neocortex	0.030 (0.004)	0.025 (0.003)	0.030 (0.004)	0.010 (0.002)
Amygdala	0.040 (0.005)	0.038 (0.005)	0.040 (0.005)	0.020 (0.003)
Olfactory bulb	0.042 (0.009)	0.029 (0.007)	0.040 (0.009)	0.008 (0.001)
Brain stem	0.088 (0.019)	0.075 (0.018)	0.099 (0.020)	0.016 (0.004)
Rest of midbrain	0.054 (0.015)	0.054 (0.015)	0.049 (0.014)	0.034 (0.010)
Basal forebrain and septum	0.029 (0.005)	0.028 (0.005)	0.026 (0.005)	0.015 (0.003)
Fimbria	0.085 (0.016)	0.078 (0.013)	0.072 (0.013)	0.043 (0.010)
Overall average	0.052 (0.010)	0.050 (0.010)	0.049 (0.010)	0.028 (0.006)